ADVANCED HEALTHCARE MATERIALS
www.advhealthmat.de

Unravelling Immune-Inflammatory Responses and Lysosomal Adaptation: Insights from Two-Photon Excited Delayed Fluorescence Imaging

Xiang Wang, Gaona Shi, Shengnan Xu, Yuansheng Sun, Hailin Qiu, Qinghua Wang, Xiaowan Han, Qingyang Zhang, Tiantai Zhang,* and Hai-Yu Hu**

Two-photon excitation (TPE) microscopy with near-infrared (NIR) emission has emerged as a promising technique for deep-tissue optical imaging. Recent developments in fluorescence lifetime imaging with long-lived emission probes have further enhanced the spatial resolution and precision of fluorescence imaging, especially in complex systems with short-lived background signals. In this study, two innovative lysosome-targeting probes, Cz-NA and *t*Cz-NA, are introduced. These probes offer a combination of advantages, including TPE (λ_{ex} = 880 nm), NIR emission (λ_{em} = 650 nm), and thermally activated delayed fluorescence (TADF) with long-lived lifetimes (1.05 and 1.71 µs, respectively). These characteristics significantly improve the resolution and signal-to-noise ratio in deep-tissue imaging. By integrating an acousto-optic modulator (AOM) device with TPE microscopy, the authors successfully applied Cz-NA in two-photon excited delayed fluorescence (TPEDF) imaging to track lysosomal adaptation and immune responses to inflammation in mice. This study sheds light on the relationship between lysosome tubulation, innate immune responses, and inflammation in vivo, providing valuable insights for the development of autofluorescence-free molecular probes in the future.

1. Introduction

Two-photon imaging has emerged as a powerful tool for investigating biological systems, offering high spatial resolution, minimal photodamage, and long-wavelength excitation (800–1000 nm) for in vitro and in vivo applications.[1–6] The use of two-photon excitation (TPE) probes with near-infrared (NIR) emissions enables deeper tissue penetration, facilitating biomolecule imaging.[7–10] However, image quality often suffers from reduced signal-to-noise ratio due to excitation light scattering and autofluorescence.[11–13] Recent advances in fluorescence lifetime imaging with long-lived emitters address these limitations by eliminating nanosecond lifetime background fluorescence and enabling microsecond to millisecond timescale signal accumulation from long-lifetime probes.[14–20] To date, two-photon excited delayed fluorescence (TPEDF) imaging, which combines TPE and delayed fluorescence, represents a pioneering approach to visualizing biological functions. However, this field remains relatively underexplored, with only one very recent publication, and it lacks in vivo imaging studies.[21]

Lysosomes, once seen primarily as digestive organelles, have emerged as intricately regulated cellular components deeply involved in inflammation and immunity regulation.[22] These dynamic organelles play a pivotal role in modulating immune-inflammatory responses, contributing to cellular homeostasis and immune processes.[23,24] Observing and studying lysosomal adaptation provide valuable insights into its role in immune-inflammatory modulation, advancing our understanding of disease pathogenesis and potential therapeutic targets.[25] Conventional lysosomal trackers have limitations hindering precise, long-term monitoring, particularly in complex in vivo systems. Thus, innovative lysosome-targeting probes are crucial for accurate, real-time lysosomal visualization in immune-inflammatory responses, in vitro and in vivo.

The naphthalimide scaffold holds promise for efficient TPE probes.[26–29] In this study, we designed two novel donor-acceptor-donor (D-A-D) type thermally activated delayed fluorescence (TADF) probes, Cz-NA and *t*Cz-NA, incorporating a rigid 1,8-naphthalimide acceptor skeleton with carbazole (Cz) or

X. Wang, G. Shi, S. Xu, Q. Wang, X. Han, Q. Zhang, T. Zhang, H.-Y. Hu
State Key Laboratory of Bioactive Substances and Function of Natural Medicine
Beijing Key Laboratory of Active Substances Discovery and Drugability Evaluation
Institute of Materia Medica
Chinese Academy of Medical Sciences & Peking Union Medical College
Beijing 100050, China
E-mail: zhangqingyang@imm.ac.cn; ttzhang@imm.ac.cn; haiyu.hu@imm.ac.cn

Y. Sun
Flourescence Products
ISS, Inc.
1602 Newton Drive, Champaign IL 61822, USA

H. Qiu
Department of Fluorescence Test Technology
Orient KOJI Ltd.
Tianjin 300122, China

The ORCID identification number(s) for the author(s) of this article can be found under https://doi.org/10.1002/adhm.202304223

DOI: 10.1002/adhm.202304223

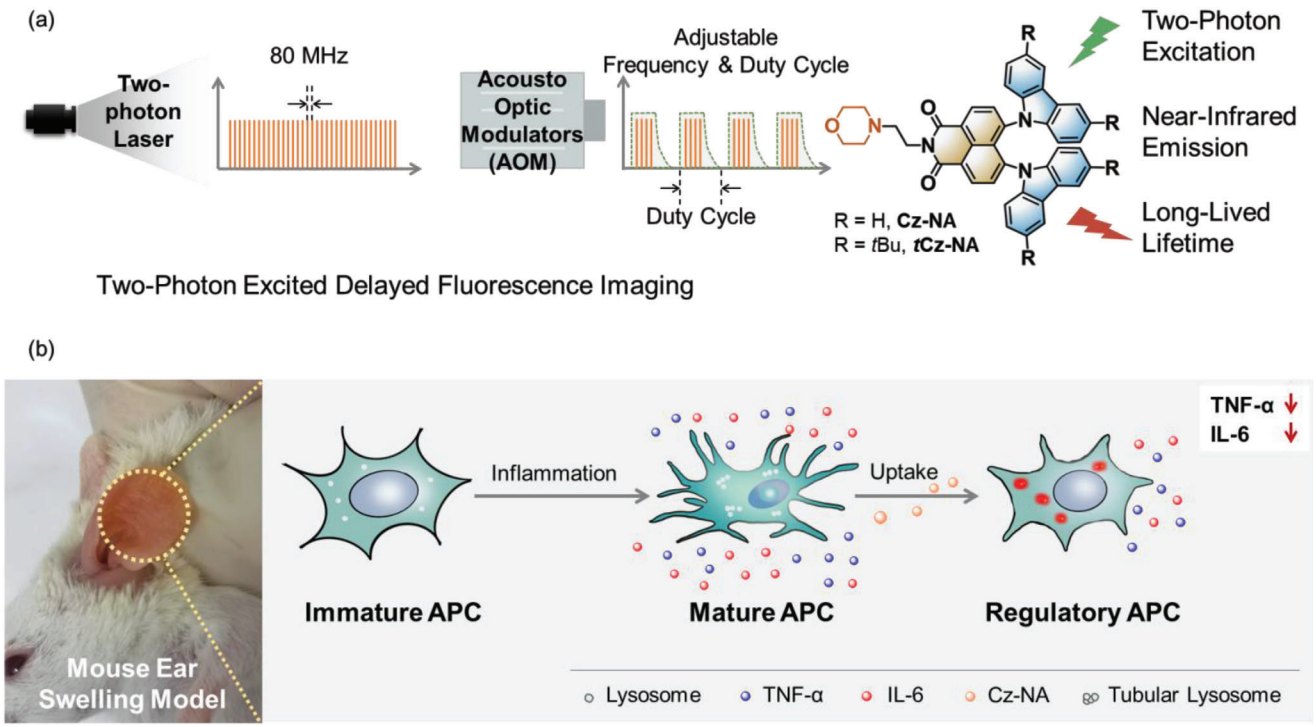

Figure 1. Schematic diagram of the a) design and b) biological applications of Cz-NA and *t*Cz-NA.

(*t*-butyl)-carbazole (*t*Cz) units as electron donors. We further incorporated the 2-morpholinoethylamine moiety to confer water solubility and enhance lysosome targeting and accumulation capabilities.[30–32] These probes exhibited large Stokes shifts of ≈200 nm, NIR emission at 650 nm, and effective separations of the highest occupied molecular orbital (HOMO) and the lowest unoccupied molecular orbital (LUMO) electron densities, resulting in small ΔE_{ST} values of 0.10 and 0.12 eV, and long luminescence lifetimes of 1.05 and 1.71 µs, respectively. To overcome the limitations of the current two-photon fluorescence lifetime imaging system, where the two-photon laser is limited to producing high-frequency single-pulsed signals (usually 80 MHz) and encounters challenges in collecting long fluorescence lifetime signals, we integrated an acousto-optic modulator (AOM) into the system. This integration allowed us to attain precise and adjustable frequency and duty cycle controls (**Figure 1a**), thereby enhancing our ability to perform effective TPEDF imaging. This improvement has significantly increased our capacity to accurately capture long-lived fluorescence signals and visualize biological events. Further, Cz-NA was successfully employed in TPEDF imaging to monitor real-time lysosomal dynamics in LPS-activated phagocytes (Figure 1b). Our results revealed significant lysosomal volume expansion and retention capacity in activated immune cells compared to resting counterparts. Additionally, we visualized substantial lysosome expansion in activated immune cells using a mouse ear swelling model-contact hypersensitivity (CHS) responses,[33] providing scientific insights into lysosome's function in immune cell activation and immune-inflammatory responses.

2. Results and Discussion

2.1. Synthesis and Characterization of Cz-NA and *t*Cz-NA

Cz-NA and *t*Cz-NA were efficiently synthesized in a single step using 2F-NA, previously prepared by our group.[19] (Scheme S1, Supporting Information). Suitable single crystals for X-ray diffraction analysis were obtained through the gradual evaporation of a Cz-NA solution in a dichloromethane and methanol mixture (1:4, v/v) (Table S1, Supporting Information). As depicted in **Figure 2a**, Cz-NA assumes a twisted conformation, characterized by two carbazole groups positioned closely to each other, featuring substantial dihedral angles of 62.7° and 64.7° in relation to the naphthalimide moiety. This twisted structure serves a dual purpose: it prevents fluorescence quenching in the aggregated state caused by intermolecular stacking and fosters effective charge separation between HOMO and LUMO, ultimately leading to delayed fluorescence. In Figure 2b, the molecular packing and various intermolecular interactions are illustrated. Adjacent molecules assemble through head-to-tail stacking, facilitated by numerous C–H···π and C–H···O interactions, while π···π stacking is conspicuously absent. These intermolecular interactions enhance rigidity and minimize nonradiative energy dissipation.

2.2. Theoretical Calculations of Cz-NA and *t*Cz-NA

To further explore the distinctions in geometric structure and electron density distribution between Cz-NA and *t*Cz-NA, we conducted molecular simulations using time-dependent density

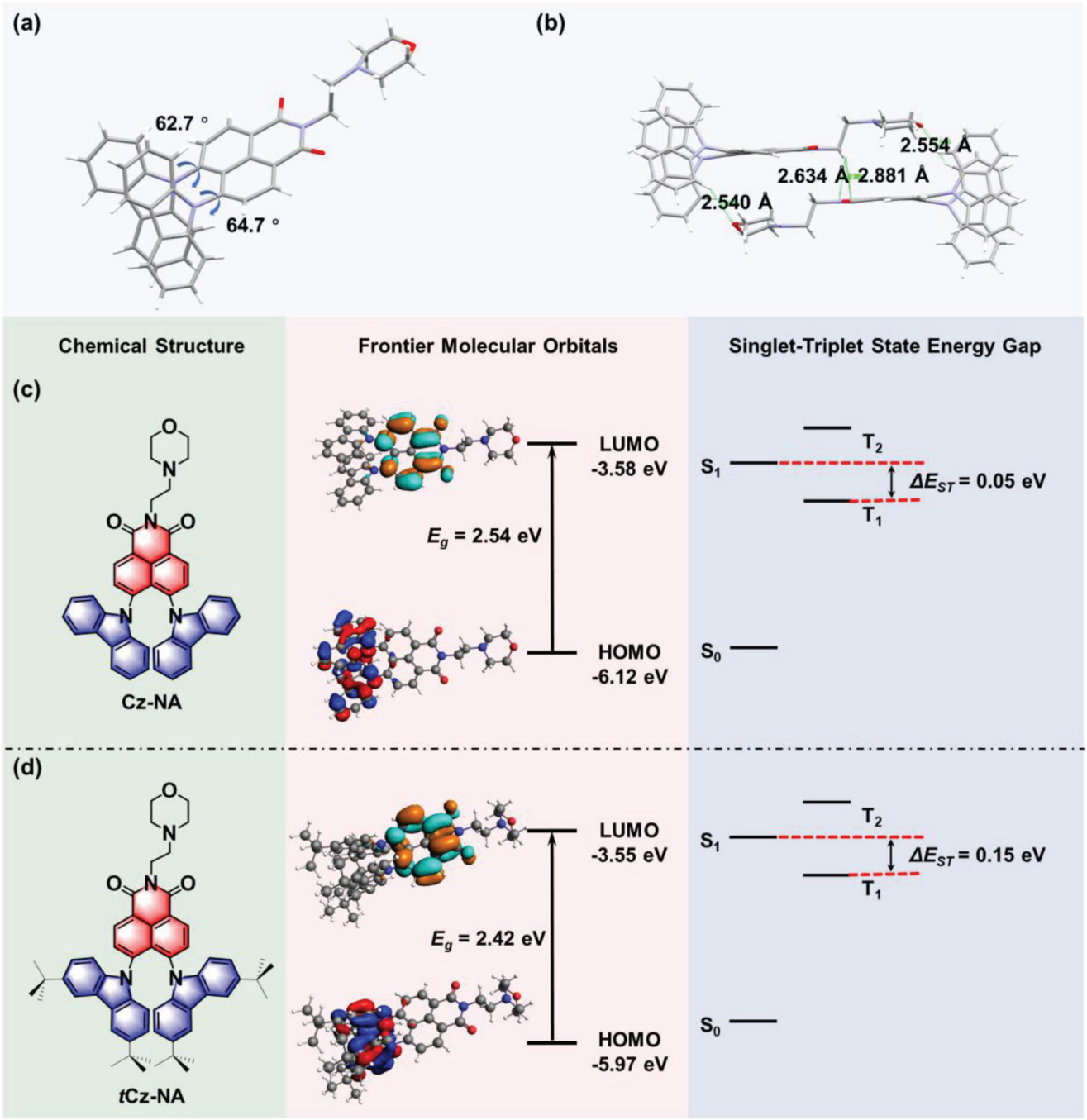

Figure 2. Crystal structures of a) Cz-NA and b) molecular packing and interactions of Cz-NA. The calculated spatial distributions of the HOMO and LUMO energy densities and energy splitting (ΔE_{ST}) between singlet and triplet states of c) Cz-NA and d) *t*Cz-NA.

functional theory (TD-DFT) within the B3LYP/TZP basis set, employing the ADF 2021 package. The computed energy levels of HOMO and LUMO, along with the optimized geometries of Cz-NA and *t*Cz-NA, were displayed in Figure 2c,d. The calculated data revealed that Cz-NA and *t*Cz-NA exhibited HOMO/LUMO energy levels of −6.12/−3.58 and −5.97/−3.55 eV, respectively, with corresponding band gaps of 2.54 and 2.42 eV. The HOMOs of Cz-NA and *t*Cz-NA primarily resided on the carbazole moiety due to their strong electron-donating capability, while the LUMOs were situated on the naphthalimide moiety, owing to its pronounced electron-withdrawing properties. This spatial electronic separation, a prominent characteristic of typical TADF molecules, effectively disrupted the electronic transition of the charge-transfer excited state and reduced ΔE_{ST}. The dihedral angles between the various carbazole donor units and the naphthalimide unit in the optimized geometries were 64.9° and 65.6°, respectively. This dihedral angle value for Cz-NA is closely aligned with those obtained from single crystal

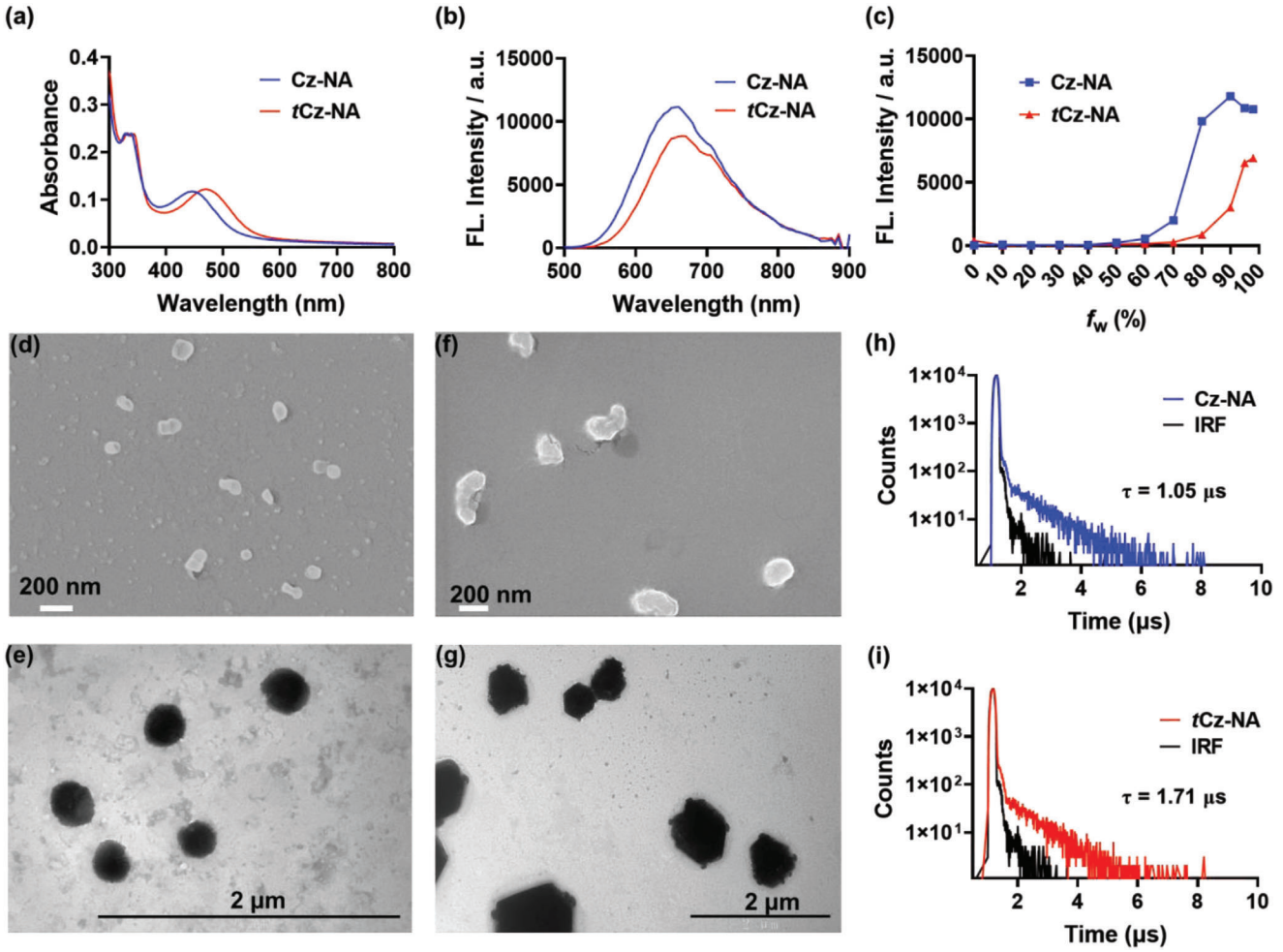

Figure 3. a) Absorption and b) fluorescence emission spectra of Cz-NA and *t*Cz-NA (20 μM) in PBS buffer (pH 7.4) with 2.0% DMSO as co-solvent. c) Fluorescence emission intensity of Cz-NA and *t*Cz-NA (20 μM) in a mixture of THF and water at different f_w. Cz-NA: λ_{em} = 655 nm; *t*Cz-NA: λ_{em} = 660 nm. Blue line: Cz-NA; red line: *t*Cz-NA. d) SEM and e) TEM images of Cz-NA. f) SEM and g) TEM images of *t*Cz-NA. Fluorescence emission decay of h) Cz-NA and i) *t*Cz-NA (20 μM) in toluene after deoxygenating. Blue line: Cz-NA; red line: *t*Cz-NA; black line: IRF. $\lambda_{ex}/\lambda_{em}$ = 475/640 nm.

analysis. Moreover, the ΔE_{ST} was typically influenced by the dihedral angle, which governs the extent of HOMO–LUMO separation.[33–35] Consequently, the calculated ΔE_{ST} values for Cz-NA and *t*Cz-NA were 0.05 and 0.15 eV using the LCY-PBE/TZP basis set, respectively, indicating efficient up-conversion from T_1 to S_1. To experimentally determine their ΔE_{ST} values, we examined the emission spectra of Cz-NA and *t*Cz-NA in oxygen-free 2-methyltetrahydrofuran (2-MeTHF) at 77 K (Figure S1 and Table S2, Supporting Information). The low-temperature emission properties yielded estimated ΔE_{ST} values of 0.10 eV for Cz-NA and 0.12 eV for *t*Cz-NA in 2-MeTHF. These experimental ΔE_{ST} values closely matched the theoretical calculations, affirming the TADF characteristics of Cz-NA and *t*Cz-NA.

2.3. Photophysical Properties Characterizations of Cz-NA and *t*Cz-NA

We conducted UV–vis absorption and fluorescence emission spectra measurements of Cz-NA and *t*Cz-NA in various solvents (Figure S2, Supporting Information). Notably, we observed negligible solvent dependence in the absorption spectra of Cz-NA and *t*Cz-NA. In solvents with differing polarities, both Cz-NA and *t*Cz-NA displayed the lowest energy absorption bands at ≈435 and 460 nm, respectively. These bands were attributed to charge-transfer absorption, primarily involving electron transfer from the carbazole moieties to the naphthalimide. Furthermore, we observed a distinct solvatochromism effect in the fluorescence emission spectra of Cz-NA and *t*Cz-NA. To investigate their suitability for biological applications, we measured the absorption and emission spectra of Cz-NA and *t*Cz-NA in phosphate-buffered saline (PBS) (**Figure** 3a,b). Cz-NA and *t*Cz-NA exhibited absorbance peaks at 445 and 470 nm, respectively, and broad fluorescence emissions with maxima at 655 and 660 nm, indicating near-infrared emissions suitable for deep tissue imaging. The small red-shift in Cz-NA and *t*Cz-NA absorption peaks in PBS (445 and 470 nm) compared to organic solvents (435 and 460 nm) is likely a result of aggregation in the PBS buffer. We determined the fluorescence quantum yields of Cz-NA and

*t*Cz-NA to be 2.06% and 1.80% in toluene using the integrating sphere method. Subsequently, we utilized Cz-NA and *t*Cz-NA for a more in-depth investigation of their aggregation-induced emission (AIE) properties. In a PBS solution, Cz-NA and *t*Cz-NA exhibited the ability to aggregate. The emission intensity of both Cz-NA and *t*Cz-NA in the THF/H_2O mixture initially decreased as the water fraction increased from f_w = 0% to 70%. However, a remarkable enhancement in emission occurred upon further increasing the water fraction from f_w = 70% to 98%. This enhancement was attributed to the restriction of intramolecular vibration in Cz-NA and *t*Cz-NA in the aggregated state (Figure 3c and Figure S3, Supporting Information). Moreover, we characterized the sizes of Cz-NA and *t*Cz-NA in water using a scanning electron microscope (SEM) and transmission electron microscope (TEM) (Figure 3d–g). The results revealed mean particle sizes of ≈150 nm for Cz-NA and ≈500 nm for *t*Cz-NA. These findings provided clear evidence of the AIE property exhibited by Cz-NA and *t*Cz-NA.

Transient photoluminescence (PL) of TADF typically comprises two components: prompt and delayed fluorescence. Notably, the lifetime of delayed fluorescence is sensitive to oxygen. To delve deeper into the TADF properties, we initially measured the PL decay curves of Cz-NA and *t*Cz-NA in toluene under oxygen-free and ambient air conditions, respectively (Figure 3h,i and Figure S4, Supporting Information). In oxygen-free toluene, both Cz-NA and *t*Cz-NA exhibited substantial delayed fluorescence with average lifetimes of 1.05 and 1.17 µs (Table S3, Supporting Information). However, in the presence of oxygen, the delayed fluorescence of both Cz-NA and *t*Cz-NA vanished, giving way to only prompt fluorescence with lifetimes of 13.01 and 11.46 ns (Figure S5 and Table S4, Supporting Information). This phenomenon exemplified the typical TADF property, where oxygen quenches triplet states, resulting in the disappearance of delayed fluorescence. Furthermore, the temperature-dependent transient PL decay spectrum of Cz-NA and *t*Cz-NA in the solid state was investigated. As the temperature rose, the lifetime of the delayed components gradually intensified, which demonstrated the TADF properties of Cz-NA and *t*Cz-NA (Figure S8a,b, Supporting Information). Meanwhile, we investigated the effect of oxygen on PL intensity (Figure S8c,d, Supporting Information). After oxygenating, the fluorescence intensity of Cz-NA and *t*Cz-NA exhibited a significant enhancement compared to Cz-NA and *t*Cz-NA under air atmosphere, demonstrating the sensitivity of fluorescence intensity to oxygen. These results demonstrated that Cz-NA and *t*Cz-NA had TADF features. Subsequently, we examined the fluorescence emission decays of Cz-NA and *t*Cz-NA in a THF/H_2O mixture with f_w = 98% and PBS (Figures S6 and S7 and Tables S5 and S6, Supporting Information). In the THF/H_2O mixture (f_w = 98%), both Cz-NA and *t*Cz-NA displayed evident delayed fluorescence with lifetimes of 2.92 and 3.63 µs, respectively. Similarly, in PBS, Cz-NA and *t*Cz-NA exhibited noticeable delayed fluorescence with lifetimes of 2.46 and 2.35 µs, respectively. These results underscored that Cz-NA and *t*Cz-NA, characterized by their aggregation-induced emission (AIE) properties, could effectively combat O_2 quenching of triplet states, thereby enhancing aggregation-induced delayed fluorescence.

2.4. One-Photon Fluorescence Intensity and Lifetime Imaging for Cz-NA In Vitro

Motivated by the favorable TADF properties observed in the solutions of Cz-NA and *t*Cz-NA, we investigated their potential for fluorescence imaging within living cells. Considering the relatively large particle size of *t*Cz-NA in aqueous solutions, we opted to focus on exploring imaging and biological applications using Cz-NA. To begin, we conducted cell viability assays for Cz-NA on macrophages (RAW 264.7) and bone marrow-derived dendritic cells (DC) using the CCK-8 kit (Figure S9, Supporting Information). Besides, as shown in Figure S10, Supporting Information, both RAW264.7 cells and DC cells exhibited no apoptosis rates after being treated with Cz-NA (10 and 20 µM) for 24 h in vitro. For the excitation and emission wavelength of Cz-NA was 488 and 650, we used the Cz-NA (10and 20 µM) sole treatment group as a negative control to exclude non-specific staining. As shown in Figure S10, Supporting Information, the percentage of 7-AAD$^+$Annexin V$^-$ cells after treated with Cz-NA (10 µM) for both RAW264.7 and DC cells was 3.58 and 4.87, and the percentage of 7-AAD$^+$Annexin V$^-$ cells after treated with Cz-NA (20 µM) for both RAW264.7 and DC cells was 6.88 and 7.09. The results revealed that exposure to Cz-NA did not induce any noticeable cytotoxic responses, indicating the low cytotoxicity and excellent biocompatibility of Cz-NA in both RAW 264.7 cells and DC. Furthermore, we aimed to establish specific staining within lysosomes. To achieve this, we conducted a colocalization study of Cz-NA in RAW 264.7 cells and DC with commercially available trackers via confocal laser scanning microscopy (CLSM). As depicted in **Figure 4a**, and Figures S11 and S12, and Tables S7 and S8, Supporting Information, Cz-NA (red channel) exhibited a high degree of overlap with Lysosome Tracker Red (green channel), as evidenced by the high Pearson's and overlap correlation coefficients.[36] This compellingly demonstrated that the fluorescence emitted by Cz-NA was primarily concentrated within the lysosomes.

Encouraged by the one-photon fluorescence imaging result obtained with Cz-NA, we proceeded to utilize Cz-NA to investigate immune-inflammatory responses and lysosomal adaptation. When activated by inflammatory factors, the endo-lysosome morphology of RAW 264.7 cells and DC undergoes a significant transformation, changing from numerous individual puncta into a tubular network. We examined the endo-lysosome morphology of these cells using CLSM imaging experiments. Initially, we pre-incubated RAW 264.7 cells and DC with Cz-NA and lysosome tracker red to ensure that the endo-lysosomes were loaded with the dye in both resting and activated cells. Subsequently, we exposed the cells to either LPS or a vehicle alone for 24 h to induce endo-lysosome tubulation and serve as a control, respectively. As depicted in Figure 4a, after 24 h of LPS activation, we clearly observed that both the endo-lysosomes of RAW 264.7 cells and DC displayed a tubular form and exhibited an expanded total endo-lysosomal volume. To substantiate this observation, we quantified the total endo-lysosome volume in LPS-activated and resting cells using fluorescence intensity analysis, leveraging the fluorescence intensity of Cz-NA and lysosome tracker red (Figure S13,

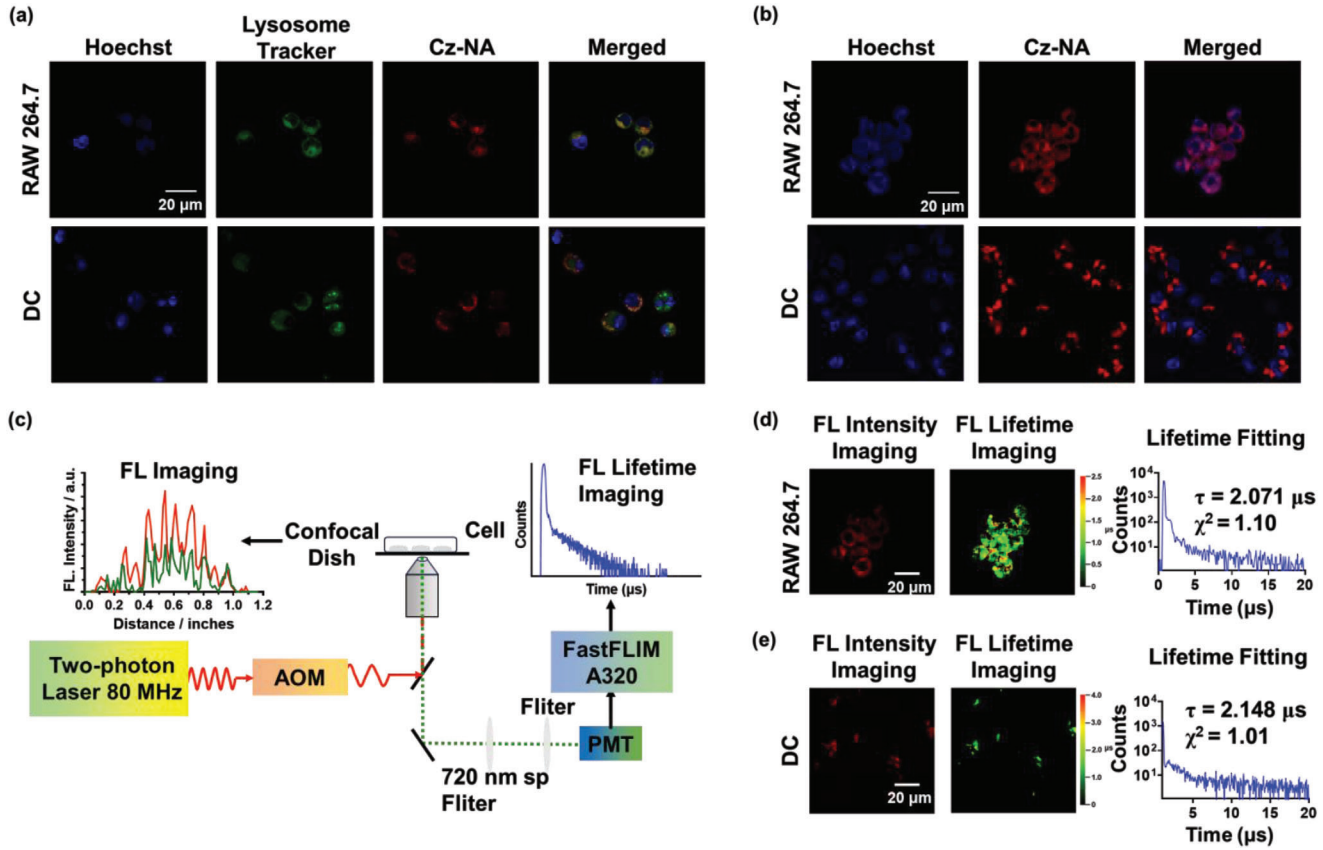

Figure 4. a) Confocal fluorescence images of Cz-NA (10 μM) in RAW 264.7 cells and DC treated with LPS for 24 h for co-localization, incubated with lysosome tracker red DND-99. Red channel for Cz-NA: $\lambda_{ex} = 488$ nm, $\lambda_{em} = 580–635$ nm. Green channel for lysosome tracker red DND-99: $\lambda_{ex} = 561$ nm, $\lambda_{em} = 580–635$ nm. Blue channel for Hoechst 33342: $\lambda_{ex} = 405$ nm, $\lambda_{em} = 420–470$ nm. Scale bar = 20 μm. b) Two-photon confocal fluorescence images of Cz-NA in RAW 264.7 cells and DC treated with LPS for 24 h. Red channel for Cz-NA: $\lambda_{ex} = 880$ nm, $\lambda_{em} = 580–635$ nm. Blue channel for Hoechst 33342: $\lambda_{ex} = 780$ nm, $\lambda_{em} = 420–470$ nm. Scale bar = 20 μm. c) The schematic of two-photon confocal microscopy for FLIM. Two-photon delayed fluorescence intensity images, delayed fluorescence lifetime images, and lifetime fitting plots of d) RAW 264.7 cells and e) DC treated with LPS for 24 h incubated with Cz-NA (10 μM). $\lambda_{ex} = 880$ nm (50 kHz repetition). Fluorescence intensity and lifetime signals were collected using a 580–635 nm filter. Scale bar = 20 μm ($n = 3$).

Supporting Information). Through fluorescence analysis, we noted a substantial increase in the fluorescence intensity of lysosomes in both RAW 264.7 cells and DC after 24 h of LPS stimulation. Additionally, DC exhibited a higher fluorescence increase than RAW 264.7 cells, indicating that DC was more sensitive than macrophages. This observation demonstrates that activated phagocytes have an increased endo-lysosomal volume relative to resting cells. Interestingly, we observed a relative decrease in fluorescence intensity with commercial lysosome tracker red in 24 h LPS-stimulated DC, which might due to different lysosomal staining mechanisms, potentially yielding misleading outcomes. Utilizing the Cz-NA probe, during the inflammatory state, we achieved clear imaging of a significant transformation of the endo-lysosomal system with the increasing fluorescence intensity of Cz-NA, transitioning from individual globular organelles to intricate tubular networks inflammation-induced lysosome activation. This result suggests that Cz-NA holds significant potential for unraveling immune-inflammatory responses and lysosomal adaptation during the inflammatory process.

2.5. Two-Photon Fluorescence Intensity and Lifetime Imaging for Cz-NA In Vitro and In Vivo

In TPEDF imaging, precise modulation of the TPE flicker frequency is crucial.[37] To meet this requirement, we established a time-resolved TPE imaging system and incorporated an AOM to control the TPE ON/OFF frequency and duty cycle. The AOM has the capacity to modulate the laser ON/OFF frequency from 1 Hz up to 1 MHz for fluorescence and phosphorescence lifetime measurements. This system allows us to precisely adjust the imaging parameters for measuring long-lived fluorescence and phosphorescence lifetimes over a wide range, from submicroseconds to hundreds of milliseconds (as illustrated in Figure 4c, additional details can be found in the Supporting Information). To demonstrate the capabilities of our system, we first investigated the phosphorescent decay curves of Cz-NA in the solid state following two-photon femtosecond laser excitation. In Figure S14, Supporting Information, we fitted the delayed fluorescence lifetime decay curve of Cz-NA using an exponential fitting model. Our findings revealed significant delayed fluorescence in the

solid state, with an average lifetime of 8.128 µs for Cz-NA. Exploiting these promising spectral properties, we conducted endo-lysosome labeling and imaging using Cz-NA in a two-photon confocal fluorescence imaging setup. We employed RAW 267.4 cells and DC for this study. As shown in Figure S15a,c, Supporting Information, the cell images labeled with Cz-NA exhibited bright red fluorescence in macrophage and DC exposed to a vehicle-alone control, which aligned well with one-photon confocal imaging. Subsequently, we stimulated the cells with LPS for 24 h and then applied Cz-NA labeling. In Figure 4b, we observed that the endo-lysosomes in both cell types had transformed into a tubular network after 24 h of LPS stimulation. Furthermore, we introduced dexamethasone (DEX), an anti-inflammatory agent, to suppress the LPS-induced stimulation. Figure S15b,d, Supporting Information showed that after adding DEX, the morphology of the endo-lysosomes reverted from a tubular network to individual puncta. This underscores Cz-NA's efficacy in endo-lysosome labeling and its capacity to visualize comprehensive endo-lysosomal volume changes during LPS stimulation via two-photon confocal imaging. Subsequently, we performed lifetime imaging using a two-photon laser scanning microscope and time-resolved phosphorescence microscopy to visualize the changes in endo-lysosomes during LPS stimulation in living macrophage and DC. Furthermore, we obtained long fluorescence lifetime signals with a mean lifetime of 2.071 µs in RAW 264.7 cells and 2.148 µs in DC when Cz-NA was incubated with cells undergoing LPS stimulation (Figure 4d,e). Additionally, long fluorescence lifetime signals with a mean lifetime of 1.894 µs in RAW 264.7 and 1.343 µs in DC were recorded when Cz-NA was incubated with cells exposed to both LPS and DEX (Figure S16, Supporting Information). Both of these show that during phagocyte activation after LPS stimulation, the lysosome undergoes an expansion in volume and capacity. These results underscore the potential of Cz-NA for tracking endo-lysosome morphology and visualizing changes in the endo-lysosomal microenvironment in inflammatory cells.

After the successful visualization of endo-lysosome changes with Cz-NA in cells, we employed this probe for monitoring the process of immune-inflammatory responses in a murine ear inflammation model in vivo (**Figure 5a**). Balb/c mice were divided into three groups, each consisting of five individuals. In two of these groups, croton oil was applied to the right ears to induce an inflammatory response, inducing an inflammatory response and activating the innate immune system.[38–41] Subsequently, one of the inflamed groups received treatment with commercially available DEX ointment (10 µg per mouse) through transdermal application, administered 30 min after the induction of inflammation.[42–44] The third group, comprised of healthy mice, served as the negative control. Cz-NA, dissolved in DMSO with 2% azone, was administered to the right ears of all three groups (10 mg kg^{-1}, 20 µl per mouse) via the transdermal route. After 4 h of croton oil stimulation, we employed two-photon confocal phosphorescence microscopy to capture time-resolved phosphorescence images in vivo and perform lifetime analysis. In Figure 5b-d, the in vivo images of Cz-NA revealed numerous bright red fluorescence signal dots in the inflamed group, whereas much fewer fluorescence signals were observed in the vehicle or DEX-treated groups. These results were further confirmed by time-resolved fluorescence imaging in investigations. As depicted in Figure S17, Supporting Information, long-lifetime signals were detected in the inflamed group, with an average lifetime of 2.054 µs. In contrast, much less long-lived fluorescence signals were found in the vehicle and DEX-treated groups. This finding indicated the recruitment of macrophages and DC to the site of inflammation. Furthermore, immunofluorescence results confirmed the co-localization of Cz-NA within lysosomes of CD11c/CD11b-positive antigen-presenting cells (Figure 5e and Figures S18 and S19, Supporting Information). These results aligned well with the above in vitro imaging.

2.6. Cz-NA Promotes Phagocytosis and Anti-Inflammatory Effect of AntigenPresenting Cells

Phagocytosis plays a pivotal role in immune cells, driving essential functions such as antigen presentation and pathogen elimination.[45,46] To assess the impact of Cz-NA on phagocytosis, we conducted in vitro experiments using the model antigen ovalbumin (OVA). The results clearly demonstrated that Cz-NA treatments (10 µM) significantly enhanced the phagocytic functions both in RAW 264.7 and DC. Additionally, macrophages treated with lower concentrations of Cz-NA (2.5 and 5 µM) also displayed a marked improvement in phagocytosis (**Figures 6**a,b, and S24, Supporting Information). Subsequently, we investigated the influence of Cz-NA on surface markers of macrophages and DC. As shown in Figure 6c, Cz-NA (10 µM) increased the percentage of $CD11b^{+}F4/80^{+}$ in macrophages. In contrast, Cz-NA (2.5 and 5.0 µM) led to a decrease in the percentage of $CD11c^{+}CD86^{+}$ and $CD11c^{+}MHCII^{+}$ DC, both in the presence and absence of LPS (1 mg ml^{-1}) in lower concentrations treated group. (Figure 6d,e and Figure S25, Supporting Information). We further delved into the anti-inflammatory properties of Cz-NA in both macrophages and DC. Irrespective of LPS treatment (1 mg ml^{-1}), Cz-NA (2.5, 5.0, and 10 µM) significantly decreased the release of IL-6 in macrophages and DC and also markedly reduced the release of TNF-α in DC (Figure 6f-h). In summary, Cz-NA exhibited significant biological functions by enhancing phagocytosis and exerting anti-inflammatory effects. Furthermore, in a mouse ear inflammation model, Cz-NA (10 mg kg^{-1}, 20 µl per mouse) demonstrated the capability to reduce ear thickness in mice treated with 1.5% croton oil, with results comparable to those achieved with the positive control, commercially available dexamethasone ointment (10 µg per mouse) (Figure 6i and Figure S26, Supporting Information).

2.7. Biosafety Assessment

Biocompatibility is essential for the in vivo biological applications of autofluorescence-free molecular probes. For the in vivo safety analysis, Cz-NA (10 and 20 mg kg^{-1}, 20 µl per mouse) was treated through a transdermal administration route on the right ears of mice for 24 h. The body weight showed no difference among all groups (Figure S23, Supporting Information) and no damage and inflammation were observed on the H&E images of the main organs (Figure S24, Supporting Information). The complete blood panel test and serum biochemistry assays (Figures S25 and S26, Supporting Information) illustrated that

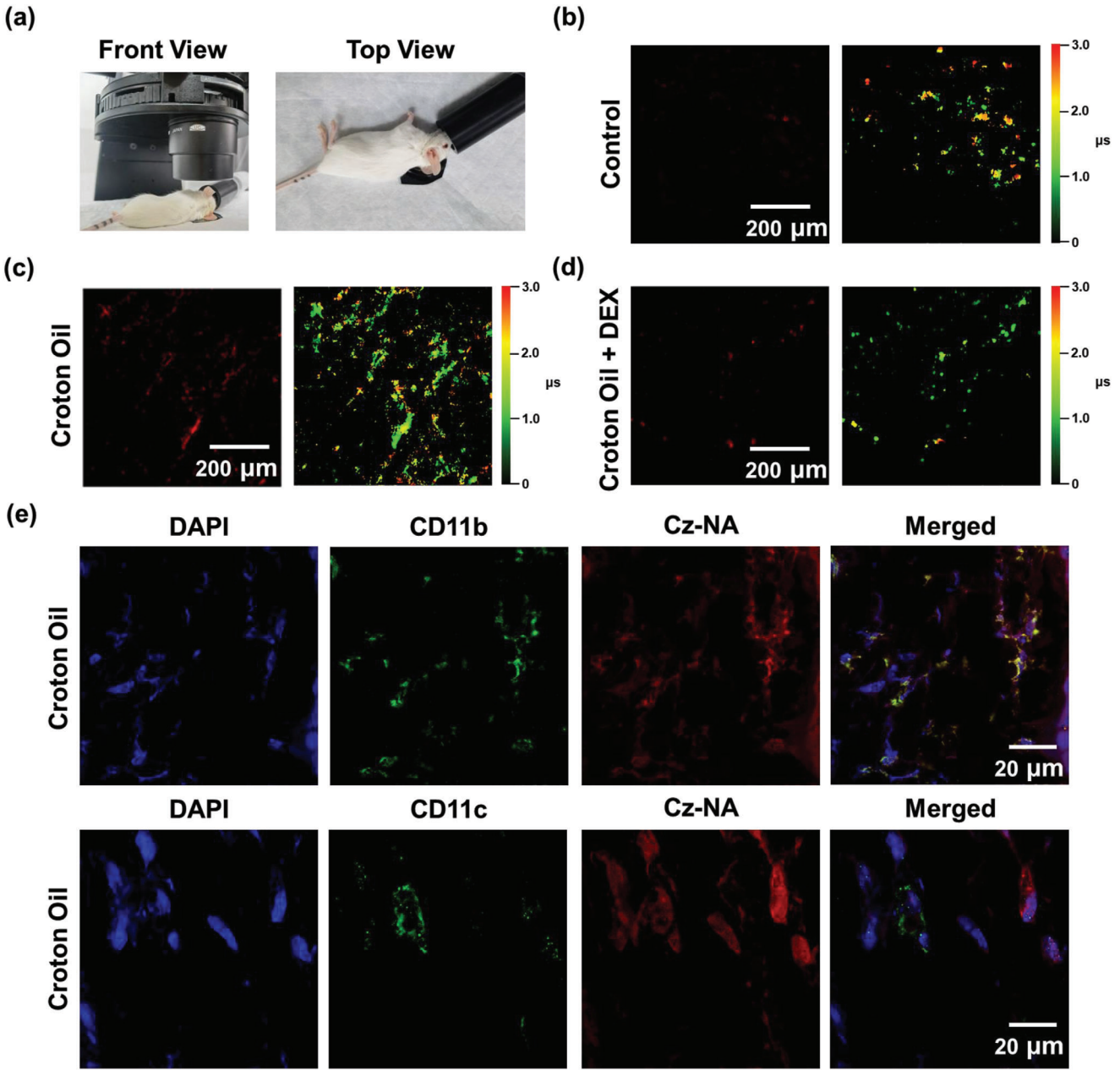

Figure 5. a) The front and top views of two-photon FLIM imaging for ear swelling mouse model in vivo. Fluorescence imaging and lifetime images of Cz-NA in b) control group, c) ear swelling mouse model group, and d) DEX-treated pinna swelling mouse model group in vivo. λ_{ex} = 880 nm, λ_{em} = 580–635 nm. Scale bar = 200 μm. e) Confocal imaging of the immunofluorescence staining of Cz-NA, CD11b, and CD11c cells in ear tissues of the pinna swelling mouse model group. Red channel for Cz-NA: λ_{ex} = 488 nm, λ_{em} = 580–635 nm. Green channel for Cd11b/CD11c: λ_{ex} = 488 nm, λ_{em} = 500–550 nm. Blue channel for DAPI: λ_{ex} = 405 nm, λ_{em} = 420–470 nm. Scale bar = 20 μm (n = 5).

Cz-NA did not cause significant changes to the key hematological parameters and serum biochemical indicators after transdermal administration. All these data confirmed that Cz-NA possessed good biocompatibility for in vivo applications.

3. Conclusion

In conclusion, we have introduced a novel two-photon excited delayed fluorescence methodology, capable of monitoring lysosomal adaptations and immune-inflammatory responses both in vitro and in vivo. This approach allows us to track the endo-lysosomal system and observe immune cells, such as macrophages and DC, transition between resting, inflammatory, and anti-inflammatory states. Notably, during the inflammatory state, we observed a remarkable transformation of the endo-lysosomal system within immune cells, transitioning from individual globular organelles to intricate tubular networks. This transformation was captured effectively through both

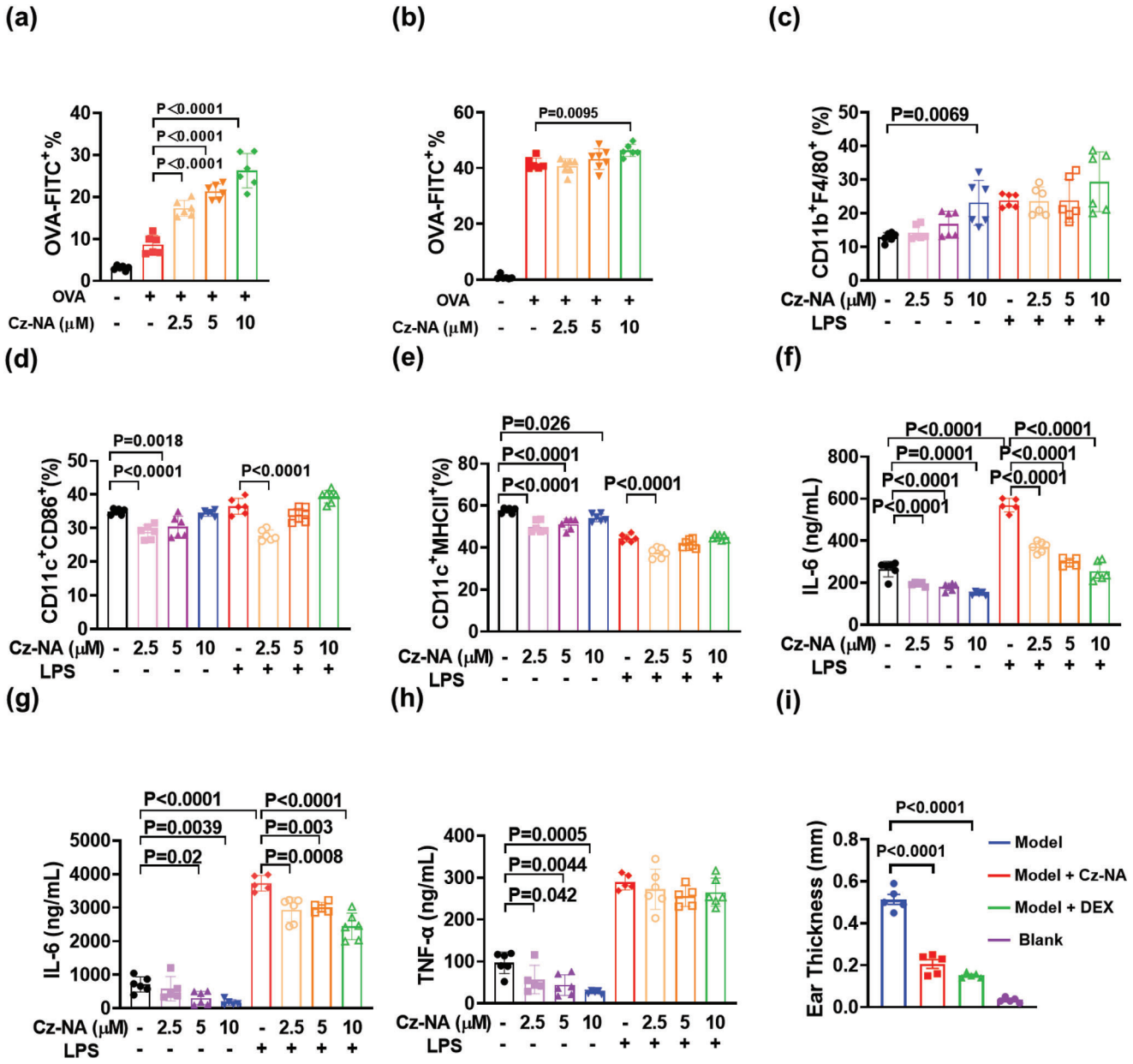

Figure 6. The biological effects of Cz-NA on inflammation and inflammatory antigen-presenting cells both in vitro and in vivo. The phagocytosis efficacy of a) RAW 264.7 and b) DC on model antigen OVA (20 μg mL^{-1}) after being treated with Cz-NA (2.5, 5.0, and 10 μM) for 24 h. c) The percentage of $CD11b^+F4/80^+$ RAW 264.7 cells after treated with Cz-NA (2.5, 5.0, and 10 μM) together with or without LPS (1 mg ml^{-1}) for 48 h. d) The percentage of $CD11c^+CD86^+$ DC after treated with Cz-NA (2.5, 5.0, and 10 μM) together with or without LPS (1 mg ml^{-1}) for 48 h. e) The percentage of $CD11c^+MHCII^+$ DC after treated with Cz-NA (2.5, 5.0, and 10 μM) together with or without LPS (1 mg ml^{-1}) for 48 h. IL-6 secretion from f) RAW 264.7 cells and g) DC after treated with Cz-NA (2.5, 5.0, and 10 μM) together with or without LPS (1 mg ml^{-1}) for 48 h. h) TNF-α secretion from DC after treated with Cz-NA (2.5, 5.0, and 10 μM) together with or without LPS (1 mg ml^{-1}) for 48 h. i) Ear thickness as a function of Cz-NA treatment in mice with ear swelling. Data are given as the mean ± SEM ($n = 5$). Statistical analysis was implemented using one-way ANOVA, followed by Dunnett's multiple comparison tests. Statistical significance values indicated as follows: ns, not significant ($p \geq 0.05$). $p < 0.05$: significant differences compared to the control group. $\Delta D = D - D_{control}$ where D is the thickness of the ear tissues with treatment and $D_{control}$ is the thickness of the other normal ear of the mouse.

one-photon and two-photon fluorescence intensity imaging using Cz-NA. Moreover, in a murine ear swelling experiment, Cz-NA proved invaluable as an in vivo probe, enabling us to visualize the recruitment of inflammatory cells, including macrophages and DC, to the swelling ear. This recruitment was further confirmed by co-staining with both CD11c and CD11b positive cell markers. Additionally, Cz-NA exhibited the capability to enhance phagocytosis and demonstrated anti-inflammatory effects in both in vitro and in vivo studies. Our findings provided an innovative imaging technology and expanded our understanding of lysosomal dynamics in activated immune cells and their pivotal role in immune cell activation and inflammatory responses.

4. Experimental Section

Synthetic Procedures and Characterized Data: Detail synthetic procedures and characterized data can be found in Supporting Information.

Theoretical Calculations of Cz-NA and tCz-NA: The geometric structures and molecular frontier orbitals of Cz-NA and *t*Cz-NA were conducted using time-dependent density functional theory (TD-DFT) within the B3LYP/TZP basis set, employing the ADF 2021 package. The calculated ΔE_{ST} values for Cz-NA and *t*Cz-NA were using the LCY-PBE/TZP basis set.

Mice and Cell Differentiation and Activation: Balb/c mice 6–8 weeks old were purchased from Beijing HFK Bioscience Co. Ltd and were housed under specific pathogen-free conditions. All animal experiments were approved by the Animal Care and Use Committee of the Institute of Materia Medica, Chinese Academy of Medical College (approval No. 00004182 and 00004194).

DC was obtained from Balb/c mice by incubating primary bone marrow cells for 7 days in RPMI 1640 (Gibco) supplemented with 1% sodium pyruvate, 50 U ml^{-1} penicillin, 50 µg ml^{-1} streptomycin, 5×10^{-5} M 2-mercaptoethanol, and 10% FBS (all from Invitrogen) supplemented with 20 ng ml^{-1} recombinant GM-CSF (PeproTech) and 10 ng ml^{-1} IL-4 (PeproTech).

The RAW 264.7 cell line used in the experiments was purchased from the ATCC Cell Resource Centre. RAW 264.7 cells were cultured in RPMI 1640 containing 10% FBS and 1% sodium pyruvate, 50 U ml^{-1} penicillin, and 50 µg ml^{-1} streptomycin, under a humidified atmosphere of 5% CO_2 at 37 °C under normoxic conditions.

Cell Viability Assays: DC and RAW 264.7 cells were incubated for 24 h with increasing amounts of Cz-NA (0.625, 1.25, 2.5, 5, and 10 µM). After incubation, cell viability was assessed with the CCK-8 kit protocol. The absorbance was measured at 450 nm with a Tecan Spark 10 M Multimode Microplate Reader. Cell viability was calculated according to the following formula: Cell viability (%) = $(A - A_{Cz\text{-}NA} - A_0) / (A_s - A_0) \times 100\%$, where A is the absorbance of the experimental group, $A_{Cz\text{-}NA}$ is the absorbance of Cz-NA at 450 nm, A_s is the absorbance of the control group, and A_0 is the absorbance of the blank group (no cells). The experiment was repeated three times for each compound.

Annexin V-FITC/7-AAD Staining: Cell apoptosis assay was tested according to the manufacturer's instructions for Annexin V-FITC/7AAD apoptosis detection kit (BioLegend, San Diego, USA). Briefly, RAW 264.7 and DC cells were seeded and grown overnight, then treated with 10 and 20 µM for 24 h. Cells were washed, collected, and resuspended with 100 µl Annexin V binding buffer containing 5 µl Annexin V-FITC and 5 µl 7-AAD for 10 min at room temperature in the dark. The fluorescence intensity of each group was analyzed within 1 h by flow cytometry (Longcyte, Challenbio, China). The data were collected to analyze the percentage of apoptosis cells.

Lysosome Colocalization Analysis of RAW 264.7 Cells and DC Incubated with Cz-NA: Colocalization experiments were conducted by co-staining the RAW 264.7 cells and DC with different treatments (vehicle, LPS [1 mg ml^{-1}], LPS+DEX [10 µM]) with appropriate combinations of Cz-NA (10 µM) for 24 h, and the corresponding commercial organelle markers (Lysosome Tracker Red DND-99 for Lysosome) for 30 min. Fluorescence imaging experiments were implemented by a Nikon Ti2U microscope using 60× magnification. Cz-NA were excited at 488 nm and the emissions were collected in the range of 580–635 nm (red); while 50 nM Lysosome Tracker Red DND-99 was excited at 561 nm and the fluorescence was monitored at 580–635 nm (green); meanwhile Hoechst 33342 was excited at 405 nm and the fluorescence was monitored at 420–470 nm (blue). The corresponding Pearson's and overlap correlation coefficients were calculated by using the software Image J.

Two-Photon Fluorescence Lifetime Imaging Microscopy (FLIM) In Vitro: Two-photon fluorescence intensity and lifetime imaging experiments were conducted by staining the RAW 264.7 cells and DC with different treatments (vehicle, LPS [1 mg ml^{-1}], LPS+DEX [10 µM]) with appropriate combinations of Cz-NA (10 µM) for 24 h. Hoechst 33342 was added to cells for 5 min. Fluorescence imaging experiments were implemented by the Nikon Ti2U microscope using 60× magnification. Cz-NA were excited at 880 nm and the emissions were collected in the range of 580–635 nm (red); meanwhile Hoechst 33342 was excited at 780 nm and the fluorescence was monitored at 420–470 nm (blue).

Mice Ear Swelling Model Induction and Lysosome Tracker Labeling: For the induction of skin inflammation, we used 20 µl 1.5% croton oil sensitization on the right mouse ears by transdermal treatment. The lysosome tracker Cz-NA in DMSO with 2% azone (10 mg kg^{-1}, 20 µl per mouse) was treated by transdermal treatment after sensitized with croton oil for 30 min, and swelling was measured after 4 h of sensitization. Mice in commercially available dexamethasone ointment as the positive control group were also transdermally treated with commercially available dexamethasone ointment (10 µg per mouse) and DMSO with 2% azone (20 µl per mouse) as negative control was treated by transdermal treatment after sensitized with croton oil for 30 min. Two-photon fluorescence imaging lifetime imaging experiments were implemented by the Nikon Ti2U microscope using 4× magnification. Cz-NA were excited at 880 nm and the emissions were collected in the range of 580–635 nm (red). The FLIM data were analyzed using the ISS VistaVision 64-bit software using an exponential decay model.

Statistical Analysis: Statistical analysis was implemented using Student's *t*-test or one-way ANOVA. All the results were analyzed with the use of Prism 7 (Prism GraphPad Software, Inc., San Diego). Analysis of flow cytometry data was performed by FlowJo 7.6.1 software (BD Biosciences, New York, USA). Data were expressed as mean ± SD for in vitro experiments and mean ± SEM for in vivo experiments. Statistical significance values were indicated as follows: ns, not significant ($p \geq 0.05$). $p < 0.05$: significant differences compared to the control group.

Supporting Information

Supporting Information is available from the Wiley Online Library or from the author.

Acknowledgements

X.W. and G.S. contributed equally to this work. The authors thank Dr. Duo Lu for his kind support of the crystal analysis of Cz-NA and for valuable discussions. This work was supported by National Natural Science Foundation of China (NSFC) projects (22277143, 22122705, 82293684, 82293680), the National Key Research and Development Program of China (2022YFE0199700), and CAMS Innovation Fund for Medical Sciences (CIFMS) (2021-I2M-1-054 and 2022-I2M-1-013)

Conflict of Interest

The authors declare no conflict of interest.

Data Availability Statement

The data that support the findings of this study are available on request from the corresponding author. The data are not publicly available due to privacy or ethical restrictions.

Keywords

fluorescence lifetime imaging, immune responses, lysosomes, near-infrared, two-photon

Received: November 29, 2023
Revised: February 17, 2024
Published online:

[1] G. S. Jayabalan, J. F. Bille, *in Encyclopedia of Modern Optics* (Eds.: B. D. Guenther, D. G. Steel), 2nd ed., Elsevier, Oxford **2018**, pp. 97–107.
[2] Y. Li, R. Tang, X. Liu, J. Gong, Z. Zhao, Z. Sheng, J. Zhang, X. Li, G. Niu, R. T. K. Kwok, W. Zheng, X. Jiang, B. Z. Tang, *ACS Nano* **2020**, *14*, 16840.
[3] V. A. Griffiths, A. M. Valera, J. Y. N. Lau, H. Roš, T. J. Younts, B. Marin, C. Baragli, D. Coyle, G. J. Evans, G. Konstantinou, T. Koimtzis, K. M. N. S. Nadella, S. A. Punde, P. A. Kirkby, I. H. Bianco, R. A. Silver, *Nat. Methods* **2020**, *17*, 741.
[4] V A. Griffiths, A M. Valera, J Yn. Lau, H. Ros, T J. Younts, B. Marin, C. Baragli, D. Coyle, G J. Evans, G. Konstantinou, T. Koimtzis, K. M. N S Nadella, S A. Punde, P A. Kirkby, I H. Bianco, R. A Silver, *Nat. Methods* **2020**, *17*, 741.
[5] M. A. Mohr, D. Bushey, A. Aggarwal, J. S. Marvin, J. J. Kim, E. J. Marquez, Y. Liang, R. Patel, J. J. Macklin, C.-Y. Lee, A. Tsang, G. Tsegaye, A. M. Ahrens, J. L. Chen, D. S. Kim, A. M. Wong, L. L. Looger, E. R. Schreiter, K. Podgorski, *Nat. Methods.* **2020**, *17*, 694.
[6] L. Wu, J. Liu, P. Li, B. Tang, T. D. James, *Chem. Soc. Rev.* **2021**, *50*, 702.
[7] M. L. Odyniec, S.-J. Park, J. E. Gardiner, E. C. Webb, A. C. Sedgwick, J. Yoon, S. D. Bull, H. M. Kim, T. D. James, *Chem. Sci.* **2020**, *11*, 7329.
[8] H.-F. Su, Q.-C. Peng, Y. U. Liu, T. Xie, P.-P. Liu, Y.-C. Cai, W. Wen, Y.-H. Yu, K. Li, S.-Q. Zang, *Biomaterials* **2022**, *288*, 121691.
[9] Q. Wang, Q. Zhang, Z. Zhang, M. Ji, T. Du, J. Jin, J.-D. Jiang, X. Chen, H.-Y. Hu, *J. Med. Chem.* **2023**, *66*, 2498.
[10] J. Ke, P. Zhao, J. Li, Q. Fu, *J. Mater. Chem. B* **2022**, *10*, 8744.
[11] J. Ackermann, J. Stegemann, T. Smola, E. Reger, S. Jung, A. Schmitz, S. Herbertz, L. Erpenbeck, K. Seidl, S. Kruss, *Small* **2023**, *19*, 2206856.
[12] J. Song, J. Kang, U. Kang, H. S. Nam, H. J. Kim, R. H. Kim, J. W. Kim, H. Yoo, *Sci. Rep.* **2023**, *13*, 14244.
[13] G. Pitruzzello, *Nat. Photonics* **2023**, *17*, 376.
[14] C.-P. Tan, Y.-M. Zhong, L.-N. Ji, Z.-W. Mao, *Chem. Sci.* **2021**, *12*, 2357.
[15] F. Ni, N. Li, L. Zhan, C. Yang, *Adv. Opt. Mater.* **2020**, *8*, 1902187.
[16] B. Brennecke, Q. Wang, Q. Zhang, H.-Y. Hu, M. Nazaré, *Angew. Chem., Int. Ed.* **2020**, *59*, 8512.
[17] X. Han, X. Meng, X. Wang, S. Leng, Q. Liu, L. Zhang, P. Li, Q. Zhang, H.-Y. Hu, *Anal. Chem.* **2023**, *95*, 7715.
[18] S. Xu, R. Wei, Z. Chen, P. Ma, G. Qiang, H. Peng, H.-Y. Hu, *Mater. Chem. Front.* **2022**, *6*, 3691.
[19] Q. Liu, M. Yang, X. Meng, X. Han, M. Nazare, Y. Xu, H.-Y. Hu, Q. Zhang, *Talanta* **2022**, *246*, 123493.
[20] S. Xu, L.-L. Wu, X. Wang, H.-Y. Hu, *TrAC, Trends Anal. Chem.* **2023**, *169*, 117356.
[21] J. B. Reyes, P. S. Sherin, A. Sarkar, M. K. Kuimova, R. Vilar, *Angew. Chem., Int. Ed.* **2023**, *62*, 2023104.
[22] D. C. Barral, L. Staiano, C. Guimas Almeida, D. F. Cutler, E. R. Eden, C. E. Futter, A. Galione, A. R. A. Marques, D. L. Medina, G. Napolitano, C. Settembre, O. V. Vieira, J. M. F. G. Aerts, P. Atakpa-Adaji, G. Bruno, A. Capuozzo, E. De Leonibus, C. Di Malta, C. Escrevente, A. Esposito, P. Grumati, M. J. Hall, R. O. Teodoro, S. S. Lopes, J. P. Luzio, J. Monfregola, S. Montefusco, F. M. Platt, R. Polishchuck, *Traffic* **2022**, *23*, 238.
[23] V. E. B. Hipolito, J. A. Diaz, K. V. Tandoc, C. Oertlin, J. Ristau, N. Chauhan, A. Saric, S. McLaughlan, O. Larsson, I. Topisirovic, R. J. Botelho, *PLoS Biol.* **2019**, *17*, 3000535.
[24] M. G. Tansey, R. L. Wallings, M. C. Houser, M. K. Herrick, C. E. Keating, V. Joers, *Nat. Rev. Immunol.* **2022**, *22*, 657.
[25] S. R. Bonam, F. Wang, S. Muller, *Nat. Rev. Drug Discovery* **2019**, *18*, 923.
[26] C. Geraghty, C. Wynne, R. B. P. Elmes, *Coord. Chem. Rev.* **2021**, *437*, 213713.
[27] H.-Q. Dong, T.-B. Wei, X.-Q. Ma, Q.-Y. Yang, Y.-F. Zhang, Y.-J. Sun, B.-B. Shi, H. Yao, Y.-M. Zhang, Q. Lin, *J. Mater. Chem. C* **2020**, *8*, 13501.
[28] C. Han, S.-B. Sun, X. Ji, J.-Y. Wang, *TrAC, Trends Anal. Chem.* **2023**, *167*, 117242.
[29] M. Yang, J. Fan, J. Zhang, J. Du, X. Peng, *Chem. Sci.* **2018**, *9*, 6758.
[30] K. Qiu, H. Zhu, T. W. Rees, L. Ji, Q. Zhang, H. Chao, *Coord. Chem. Rev.* **2019**, *398*, 113010.
[31] H. Yu, Y. Guo, W. Zhu, K. Havener, X. Zheng, *Coord. Chem. Rev.* **2021**, *444*, 214019.
[32] X. Duan, Q. Tong, C. Fu, L. Chen, *Bioorg. Chem.* **2023**, *140*, 106832.
[33] A. D. Christensen, C. Haase, *APMIS* **2012**, *120*, 1.
[34] S. Xu, Y. Duan, B. Liu, *Adv. Mater.* **2022**, *32*, 1903530.
[35] Z. Zhao, H. Zhang, J. W. Y. Lam, B. Z. Tang, *Angew. Chem., Int. Ed.* **2020**, *59*, 9888.
[36] Q. Zhang, S. Xu, M. Li, Y. Wang, N. Zhang, Y. Guan, M. Chen, C.-F. Chen, H.-Y. Hu, *Chem. Commun.* **2019**, *55*, 5639.
[37] G. Yellen, R. Mongeon, *Curr. Opin. Chem. Biol.* **2015**, *27*, 24.
[38] A. O. B. P. B. Martinsa, L. B. Rodriguesb, F. R. A. S. Cesáriob, M. R. C. Oliveirab, C. D. M. Tintinob, F. F. Castrob, I. S. Alcântarab, M. N. M. Fernandesb, T. R Albuquerqueb, M. S. A. Silvab, A. A. S. Araújod, L. J. Q. Júniurd, J. G. M. Costac, I. R. A. Menezesb, A. G. Wanderley, *Biomed. Pharmacother.* **2017**, *96*, 384.
[39] T. Vogl, M. Eisenblätter, T. Völler, S. Zenker, S. Hermann, P. Lent, A. Faust, C. Geyer, B. Petersen, K. Roebrock, M. Schäfers, C. Bremer, J. Roth, *Nat. Commun.* **2014**, *5*, 4593.
[40] Z. Liu, T. Yago, N. Zhang, S. R. Panicker, Y. Wang, L. Yao, P. Mehta-D'souza, L. Xia, C. Zhu, R. P. McEver, *Nat. Commun.* **2017**, *8*, 15196.
[41] M. Gábor, *Methods Mol. Biol.* **2003**, *225*, 129.
[42] E. Wyler, J. M. Adler, K. Eschke, G. T. Alves, S. Peidli, F. Pott, J. Kazmierski, L. Michalick, O. Kershaw, J. Bushe, S. Andreotti, P. Pennitz, A. Abdelgawad, D. Postmus, C. Goffinet, J. Kreye, S M. Reincke, H. Prüss, N. Blüthgen, A. D. Gruber, W. M. Kuebler, M. Witzenrath, M. Landthaler, G. Nouailles, *J. Trimpert Mol. Ther.* **2022**, *30*, 1952.
[43] S. Sellner, S. Kocabey, T. Zhang, K. Nekolla, S. Hutten, F. Krombach, T. Liedl, M. Rehberg, *Biomaterials* **2017**, *134*, 78.
[44] J. H. Graversen, P. Svendsen, F. Dagnæs-Hansen, J. Dal, G. Anton, A. Etzerodt, M. D. Petersen, P. A. Christensen, H. J Møller, S. K Moestrup, *Mol. Ther.* **2012**, *20*, 1550.
[45] M. Guilliams, F. Ginhoux, C. Jakubzick, S. H. Naik, N. Onai, B. U. Schraml, E. Segura, R. Tussiwand, S. Yona, *Nat. Rev. Immunol.* **2014**, *14*, 571.
[46] B. Suresh, A. Saminathan, K. Chakraborty, M. Zajac, C. Cui, L. Becker, Y. Krishnan, *PNAS* **2021**, *118*, 2113174118.